Co-assembly and multicomponent hydrogel formation upon mixing nucleobase-containing peptides

Tristan Giraud, Sabine Bouguet-Bonnet, Marie-José Stébé, Lionel Richaudeau, Guillaume Pickaert, Marie-Christine Averlant-Petit, Loic Stefan

Nanoscale

PAPER

View Article Online
View Journal

Cite this: DOI: 10.1039/d1nr02417e

Co-assembly and multicomponent hydrogel formation upon mixing nucleobase-containing peptides†

Tristan Giraud, [a] Sabine Bouguet-Bonnet, [b] Marie-José Stébé, [c] Lionel Richaudeau, [d] Guillaume Pickaert, [a] Marie-Christine Averlant-Petit [a] and Loic Stefan *[a]

Peptide-based hydrogels are physical gels formed through specific supramolecular self-assembling processes, leading to ordered nanostructures which constitute the water entrapping scaffold of the soft material. Thanks to the inherent properties of peptides, these hydrogels are highly considered in the biomedical domain and open new horizons in terms of application in advanced therapies and biotechnologies. The use of one, and only one, native peptide to formulate a gel is by far the most reported approach to design such materials, but suffers from several limitations, including in terms of mechanical properties. To improve peptide-based hydrogels interest and give rise to innovative properties, several strategies have been proposed in the recent years, and the development of multicomponent peptide-based hydrogels appears as a promising and relevant strategy. Indeed, mixing two or more compounds to develop new materials is a much-used approach that has proven its effectiveness in a wide variety of domains, including polymers, composites and alloys. While still limited to a handful of examples, we would like to report herein on the formulation and the comprehensive study of multicomponent hybrid DNA-nucleobase/peptide-based hydrogels using a multiscale approach based on a large panel of analytical techniques (*i.e.*, rheometry, proton relaxometry, SAXS, electronic microscopy, infrared, circular dichroism, fluorescence, Thioflavin T assays). Among the six multicomponent systems studied, the results highlight the synergistic role of the presence of the two complementary DNA-nucleobases (*i.e.*, adenine/thymine and guanine/cytosine) on the co-assembling process from structural (*e.g.*, morphology of the nanoobjects) to physicochemical (*e.g.*, kinetics of formation, fluorescence properties) and mechanical (*e.g.*, stiffness, resistance to external stress) properties. All the data confirm the relevance of the multicomponent peptide-based approach in the design of innovative hydrogels and bring another brick in the wall of the understanding of these complex and promising systems.

Received 16th April 2021,
Accepted 27th May 2021

DOI: 10.1039/d1nr02417e

rsc.li/nanoscale

Introduction

Over the last twenty years, peptide-based hydrogels, a class of bio-inspired supramolecular gels able to immobilize a large quantity of aqueous media (*e.g.*, water, buffers, cell culture media), have attracted particular attention in the domain of soft matter. Shorter than proteins, peptides (mainly size ranging from 1 to 20 amino acids) can act as low molecular weight gelators thanks to their propensity to self-assemble through a hierarchical assembly process involving specific intermolecular low energy interactions, including hydrogen bonds, van der Waals and electrostatic forces, π–π interactions and/or hydrophobic affinity.[1,2] Peptides are excellent candidates to design soft materials because of their high modularity in terms of sequence (*i.e.*, number, nature (*e.g.*, acidic, basic, aromatic, aliphatic) and position of the amino acids) and their inherent properties of biocompatibility, biodegradability and generally of non-immunogenicity.[3,4] These latter are key advantages for applications in a biological context and peptide-based hydrogels have been consequently reported for regenerative medicine, tissue engineering, controlled release of bioactive compounds (*e.g.*, growth factors, antibiotics, mRNA, IgG), MRI imaging and adjuvants for vaccines.[5–7] Other technological applications for the immobilization of biocatalysts,

[a]Université de Lorraine, CNRS, LCPM, F-54000 Nancy, France. E-mail: loic.stefan@univ-lorraine.fr
[b]Université de Lorraine, CNRS, CRM2, F-54000 Nancy, France
[c]Université de Lorraine, CNRS, IJB, F-54000 Nancy, France
[d]Université de Lorraine, CNRS, L2CM, F-54000 Nancy, France

†Electronic supplementary information (ESI) available. See DOI: 10.1039/d1nr02417e

the production of nanostructured silica, the encapsulation of carbon nanotubes or the removal of toxic dyes and metals from wastewater complete this list and confirm the relevance of such systems.[8] Interestingly, the overwhelming majority of peptide-based hydrogels are monocomponent, formulated with only one peptide derivative.[2,7] In order to optimize and/or bring new properties to the material, various modifications have been brought to the peptide sequences,[8,9] including the incorporation of large aromatic moieties (*e.g.*, Fmoc, naphthyl),[10] aliphatic chains, halogen atoms[11] or pseudopeptide bonds[12–14] to name a few. To overcome some inherent limitations of monocomponent peptide-based hydrogels and to give rise to innovative properties, the development of multicomponent peptide-based hydrogels has recently appeared as a promising and relevant strategy.[15,16] Mixing two or more compounds to develop new materials is a well-documented approach that has proven its effectiveness in a wide variety of domains, including polymers,[17,18] metal organic frameworks,[19] composites[17] or alloys. However, because of the diversity of co-assemblies peptide derivatives can adopt (*e.g.*, orthogonal, cooperative, random or destructive co-assemblies),[16,20] multicomponent peptide-based hydrogels are complex to design and to characterized,[21] and their properties difficult to predict, limiting their potential. Thus, they are still restricted to a handful of examples, following five main strategies:

(i) *Peptide[A] + peptide[A] functionalized with biologically relevant motifs*: These hydrogels are comprised of a mixture of a self-assembling peptide and the same peptide functionalized with biological recognition motifs to bring additional properties. For instance, the 16-mer EAK16-II mixed with its histidinylated analogue favours for the anchoring and the aggregation of epithelial cells,[22] while the RADA-16 peptide has been co-assembled with a wide variety of RADA-16 functionalized with integrin-binding,[23] laminin,[24] or bone marrow homing[25] motifs.

(ii) *Peptide[A] + peptide[A]-linker-peptide[A]*: To improve cross-linking between fibrils, a self-assembling peptide can be mixed with a longer one comprised of two sequences of the same peptide, linked by a spacer. Thus, doping the 8-mer FEKII with various quantities of FEKII-Glu_2-FEKII modulates the resulting hydrogel properties with an increase of the storage modulus from 80 to 2400 Pa.[26] Similarly, 17 weight% of SA5N-Glu-Val-Pro-$(Glu\text{-}Val)_2$-Pro-Glu-Val-Glu-SA5N improve the stiffness of the gel formed by SA5N alone by a factor of ~2.[27]

(iii) *Fmoc-peptide[A] + (Fmoc)-peptide[B]*: Very short peptides protected at their N-term by a Fmoc moiety have been extensively studied for their ability to form hydrogels[1,28] and are undoubtedly the most studied compounds for multicomponent peptide-based hydrogels.[28–31] For instance, an equimolar mixture of Fmoc-Phe-Phe and Fmoc-^{F5}Phe can form a hydrogel with mechanical properties 20× and 6× greater than each individual compound, respectively.[32] Similarly, playing with the Fmoc-Phe-Phe/Fmoc-Ser ratio allows a modulation of the gel stiffness from 0.1 to 32 kPa with applications in cell culture.[33]

(iv) *Enantiomeric peptide mixtures*: While native peptides and proteins are comprised of L-amino acids, the use of D-peptides has been proposed as another strategy to design multicomponent peptide-based hydrogels. Thus, the enantiomeric mixture of the 20-mer MAX1 with ^{D}MAX1 is 4× more rigid than the single L-enantiomer-containing hydrogel.[34] The equimolar mixture of L-Ac-$(Phe\text{-}Glu\text{-}Phe\text{-}Lys)_2$-$NH_2$ with D-Ac-$(Phe\text{-}Glu\text{-}Phe\text{-}Lys)_2$-$NH_2$ also exhibits an improvement of the gel stiffness compared with each enantiomer alone, and better stability against proteolysis than the L-peptide alone.[35]

(v) *Oppositely charged peptides*: Exploiting the weak interactions favouring the peptides assembly, multicomponent peptide-based hydrogels can be formed *via* the co-assembly of oppositely charged peptides, thanks to, *inter alia*, ion pair formation. Thus, several systems have been developed,[36,37] including the Cbz-$(Phe\text{-}Asp)_2$-NH-C_3H_7 + Cbz-$(Phe\text{-}Lys)_2$-NH-C_3H_7 mixture,[38] or the Glu_2-Phe-Lys-Trp-Lys-Phe-Lys-Glu_2 and Lys_2-Phe-Glu-Trp-Glu-Phe-Glu-Lys_2 blend for which the storage moduli of the gel can be modulated from 0.1 to 100 kPa, depending on both the pH and concentration of the sample.[39]

All these examples, based on five main strategies even if not exhaustive,[20,40–42] confirm the potential of the multicomponent peptide-based hydrogels, with the possibility to control the sol/gel transitions and to fine-tune the physicochemical properties of the soft matter, in order to fit with the intended applications. In any case, hydrogels formulated from multicomponent co-assembly seem to offer a synergy of their properties, which become greater than the sum of their parts. To gain further insights into the development of multicomponent peptide-based hydrogels, we would like to report herein on the ability of nucleobase-containing peptides to form stable multicomponent hydrogels at physiological pH. While the incorporation of nucleobases into peptide sequences to develop monocomponent hydrogels has only been scarcely considered, with only a dozen of reported examples,[43] their use for multicomponent hydrogels is even rarer. Thus, the Xu group focused on the self-assembling Phe-Phe(-Tyr)[44] and on the co-assembling (Lys-)Thr-Thr-Pro-Val/Leu-Gly-Phe-Asn-Ile[45,46] peptides, for which one nucleobase was grafted at their N-term. When two peptides containing complementary nucleobases adenine and thymine were mixed, an improvement of the mechanical properties was observed. A similar observation was reported by the Suggs group with the Phe_3 peptide functionalized with one nucleobase at its N-term.[47] Meanwhile, the Nilsson group described a complex system involving three peptides (with two of them functionalized with 10-mer nucleic acids) for which the addition of an extra single-stranded DNA improves the gel stiffness.[48] Additionally, the Stupp group developed two 9-mer peptides containing an alkyl chain and complementary oligonucleotides (from 10 to 45 nucleobases) at their N- and C-term, respectively,[49] and their mixture leads to the formation of stiff reversible hydrogels with tuneable mechanical properties thanks to the use of specific extra single-stranded DNA. These examples highlight that the use of hybrid nucleobase-containing peptides to form multicomponent hydrogels, while

highly promising, is still at its infancy. For these reasons, we report herein on the multiscale study of six multicomponent hydrogels formed by the mixture of heptapeptides functionalized at their N-term by one peptide nucleic acid. The resulting hydrogels exhibit higher mechanical properties (stiffness, resistance to stress), better abilities to constrain water molecules, faster kinetics of formation and better propensity to form fibrillar architectures when the peptides containing two complementary nucleobases (*i.e.*, adenine + thymine and guanine + cytosine) are combined.

Results and discussion

Design, synthesis, and co-assembly mixtures conditions

To study multicomponent nucleobase-containing peptide-based hydrogels, we focus herein on five compounds built from the heptapeptide H_2N-Glu-(Phe-Glu)$_1$-(Phe-Lys)$_2$-OH, derived from the octapeptide H_2N-(Phe-Glu)$_2$-(Phe-Lys)$_2$-OH first reported by the Saiani group,[50,51] and functionalized at its N-term by a peptide nucleic acid (also termed PNA) to introduce the nucleobases. PNA are synthetic DNA equivalents in which the phosphate-ribose moiety is substituted by a peptide backbone being, most commonly, a *N*-(2-aminoethyl)glycine (acronym = Aeg). They also offer a better chemical stability and a reduction of non-specific electrostatic repulsions thanks to the absence of charges, and they form more stable duplex assemblies, making PNA good alternatives for biomedical applications[52] and in materials science.[53] Thus, we synthesized at a 400 μmol-scale the four compounds **PNA(X)-pep** with **X** = adenine (**A**), thymine (**T**), cytosine (**C**) or guanine (**G**) and, for the sake of comparison, the nucleobase-lacking equivalent **Aeg-pep** (Fig. 1a) (see the Material and methods section for details on the synthesis and purifications). **PNA(X)-pep** are a series of hybrid nucleopeptides forming monocomponent hydrogels (at 15 mM, pH 7.4) for which, *inter alia*, mechanical and physicochemical properties can be modulated and fine-tuned as a function of the nature of the nucleobase.[54] To take a further step toward the understanding of such self-assembling systems and to harness the recognition behaviour of nucleobases, we provide a multiscale analysis of multicomponent hydrogels in which two nucleopeptides are mixed together. As previously considered for nucleobase-containing peptides[44,45,47] and due to the nucleobase-pairing ability, we studied multicomponent mixtures containing two compounds in an equimolar ratio (1 : 1), and at a total concentration of 15 mM, *i.e.*, all the samples we prepared contain 7.5 mM of each peptide derivative (corresponding to 0.8–1.0 wt%, depending on the nucleopeptide). A total concentration of 15 mM has been selected because it allows: (i) the gelification of the large majority of the mixtures in a reasonable amount of time and (ii) a direct comparison with the properties of numerous already reported peptide-based hydrogels.[11,55–57] Interestingly, contrary to numerous hydrogels that require a pre-solubilisation in organic solvent (mainly DMSO),[27,58–60] no additional solvent has to be used for the formulation of our *stricto sensu* hydrogels.

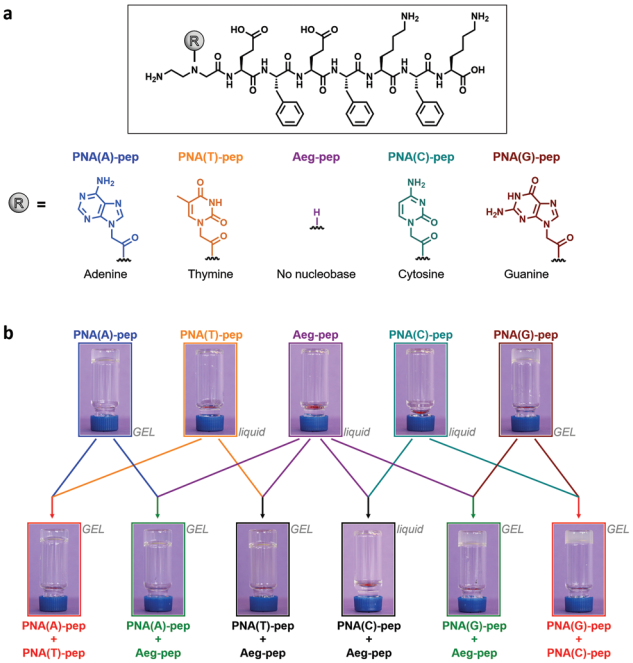

Fig. 1 (a) Chemical structures of the hybrid DNA-nucleobase/peptide derivatives and the DNA-nucleobase-lacking peptide (**Aeg-pep**). (b) Photographs of all the mixtures forming (or not) hydrogels. The six equimolar multicomponent mixtures at the bottom are the main focus of this work.

Macroscopic scale: visual aspects and tube inversion tests

The tube inversion test is an often-used method to visually check the ability of a system to form (or not) a gel and to evaluate the sol/gel transition time ($t_{s/g}$) at which the sample starts to be self-supporting after its formulation. Using this test, we observed (Fig. 1b and Table 1) the formation of homogeneous translucent hydrogels for **PNA(A)-pep** and **PNA(G)-pep** alone with $t_{s/g}$ = 13 min and 70 min, respectively, whereas the three other **PNA(T)-pep**, **PNA(C)-pep** and **Aeg-pep** failed to gel even after six months (Table S1†). Considering equimolar mixtures, the two complementary nucleobase-containing **PNA(A)-pep** + **PNA(T)-pep** form a transparent self-supporting hydrogel in 5 min, faster than **PNA(A)-pep** or **PNA(T)-pep** in the presence of the nucleobase-lacking **Aeg-pep** which require 10 and 20 min, respectively (Table 1). In parallel, the two complementary nucleobase-containing **PNA(G)-pep** + **PNA(C)-pep** mixture has the fastest $t_{s/g}$ (*i.e.*, 2 min, Table 1) of the studied mixtures, better than **PNA(G)-pep** + **Aeg-pep** and **PNA(C)-pep** + **Aeg-pep**. This latter still has a viscous liquid aspect after three months (Table S1†). Altogether, these visual macroscopic examinations point out that the presence of the complementary nucleobases (*i.e.*, adenine (A) + thymine (T), guanine (G) + cytosine (C)) has positive effects on the sol/gel transition time and on the qualitative hydrogel behaviour (*e.g.*, stiffness), better than all the

Table 1 Characteristic macroscopic and rheological properties of all the six equimolar mixtures studied at 7.5 mM of each compound in Tris·HCl (1 M, pH 7.4)

	Sol/gel transition time $t_{s/g}$	Macroscopic aspect	Gelification time t_{gel^*}	Storage modulus G' (Pa)	Loss modulus G'' (Pa)	Yield point τ_y (Pa)	Initial stiffening rate V_0 (Pa min^{-1})
PNA(A)-pep + PNA(T)-pep	**5 min** (±2 min)	Translucent gel	**272 min** (±8 min)	**5803** (dev. std. 304)	**263** (dev. std. 13)	**131** (dev. std. 6.7)	**82.5** (dev. std. 1.6)
PNA(A)-pep + Aeg-pep	**10 min** (±2 min)	Clear gel	**236 min** (±12 min)	**2891** (dev. std. 759)	**108** (dev. std. 26)	**73.3** (dev. std. 9.2)	**0.68** (dev. std. 0.04)
PNA(T)-pep + Aeg-pep	**20 min** (±3 min)	Clear gel	**>360 min**	**412** (dev. std. 135)	**15.3** (dev. std. 3.4)	**25.7** (dev. std. 2.3)	**1.05** (dev. std. 0.05)
PNA(G)-pep + PNA(C)-pep	**2 min** (±1 min)	Translucent gel	**212 min** (±8 min)	**6794** (dev. std. 866)	**559** (dev. std. 61)	**59.0** (dev. std. 4.3)	**585** (dev. std. 6.9)
PNA(G)-pep + Aeg-pep	**8 min** (±2 min)	Clear gel	**216 min** (±8 min)	**3077** (dev. std. 208)	**230** (dev. std. 18)	**30.6** (dev. std. 1.7)	**57.2** (dev. std. 0.9)
PNA(C)-pep + Aeg-pep	**>4 days**	Liquid	**276 min** (±12 min)	**28.3** (dev. std. 10.8)	**7.0** (dev. std. 3.3)	**<1**	**0.44** (dev. std. 0.10)

compounds alone and than all the equivalent mixtures containing **Aeg-pep**.

Macroscopic scale: mechanical properties

To assess quantitative values of all these multicomponent systems, we performed a series of rheological investigations for the six mixtures and the five compounds alone, in triplicate to ensure the reproducibility of the experiments. Thus, time-dependant rheological measurements were carried out, and the results are reported Fig. 2a, b, 3a, b and Table 1 (see also Fig. S1, S2 and Table S2†). On the one hand, while **PNA(A)-pep** has a storage modulus of 55 Pa after 6 hours (Table S2†), the presence of **PNA(T)-pep** (which fails to form a gel alone) drastically improves the gel stiffness by a factor >100, with G' = 5803 Pa for the **PNA(A)-pep** + **PNA(T)-pep** mixture (Table 1). Interestingly, when **Aeg-pep** is added to **PNA(A)-pep** or to **PNA(T)-pep**, the resulting gels are weaker with storage moduli of 2891 Pa and 412 Pa, respectively. On the other hand, the same trend occurs with **PNA(G)-pep** + **PNA(C)-pep** which forms a strong gel (G' = 6794 Pa), far better than the ones in the presence of **Aeg-pep** (see Table 1 and Fig. 3a, b), and 8.2-fold better than **PNA(G)-pep** alone (*nota*: and also better than **PNA(C)-pep** alone which is a solution). These rheological results first confirm the visual observations we made using the tube inversion tests (*vide supra*) and highlight that the two multicomponent systems containing the complementary bases A + T and C + G are the stiffest hydrogels, confirming their collaborative effect on the mechanical properties. Interestingly, while the two equimolar mixtures do not show significant thixotropic behaviour (data not shown) contrasting with the monocomponent hydrogels previously reported,[54] they exhibit excellent thermo-reversibility without loss of mechanical properties even after five cycles of heating/cooling (Fig. S3†). Additionally, playing with the ratio of each component in the mixture (*i.e.*, 0.25/0.75 and 0.75/0.25 instead of 1/1) allows a drastic modulation of the mechanical properties as observed *via* time, frequency and stress sweep experiments (Fig. S4–S6 and Table S3†). Exploiting the time-dependent rheograms to determine kinetic properties, we first observe that the time G′ requires to reach a plateau (*i.e.*, the time at which the gelification process is completed, termed t_{gel^*}, Table 1) is ranging from 210 to 280 min, except for PNA(T)-pep + Aeg-pep. Moreover, the initial stiffening rates, corresponding to the increase of the storage modulus as a function of time in the first 5 min, were calculated. As depicted Fig. 3c, the fastest initial rate is obtained for the **PNA(G)-pep** + **PNA(C)-pep** mixture, with V_0 = 585 Pa min^{-1}, *i.e.*, ∼10 and ∼1000 times higher (Table 1) than **PNA(G)-pep** or **PNA(C)-pep** in the presence of **Aeg-pep**, respectively. Similarly, the hydrogel formation for **PNA(A)-pep** + **PNA(T)-pep** is more than 80-fold quicker than the other blends comprising both the adenine or the thymine derivative and the **Aeg-pep** one (Fig. 2c and Table 1). These results, consistent with our qualitative tube inversion tests (*vide supra*), reveal that the stiffest multicomponent gels are also hierarchically the fastest ones, as previously reported for other systems[1,61] even if it is not always the case[62,63] as

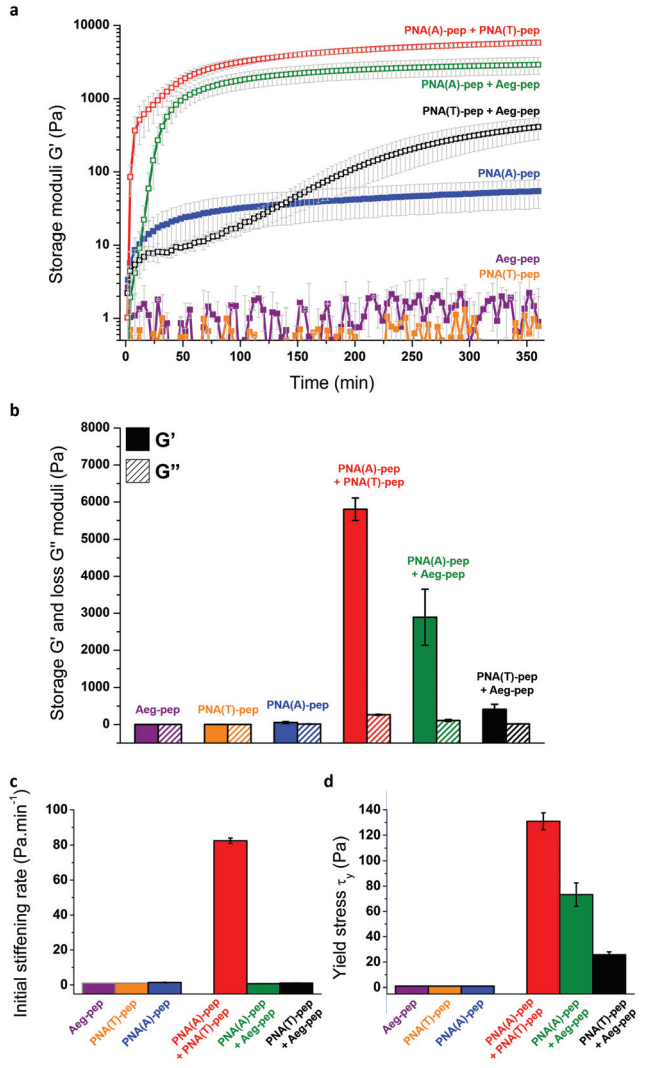

Fig. 2 (a) Time sweep rheological profiles and (b) plot of the resulting storage (G') and loss (G'') moduli after 6 hours. Plot of the characteristic (c) initial stiffening rate V_0 and (d) limiting values of the linear viscoelastic region (yield stress τ_y). All the experiments were carried out with **PNA(A)-pep**, **PNA(T)-pep** and/or **Aeg-pep** at 7.5 mM of each compound in Tris·HCl (1 M, pH 7.4).

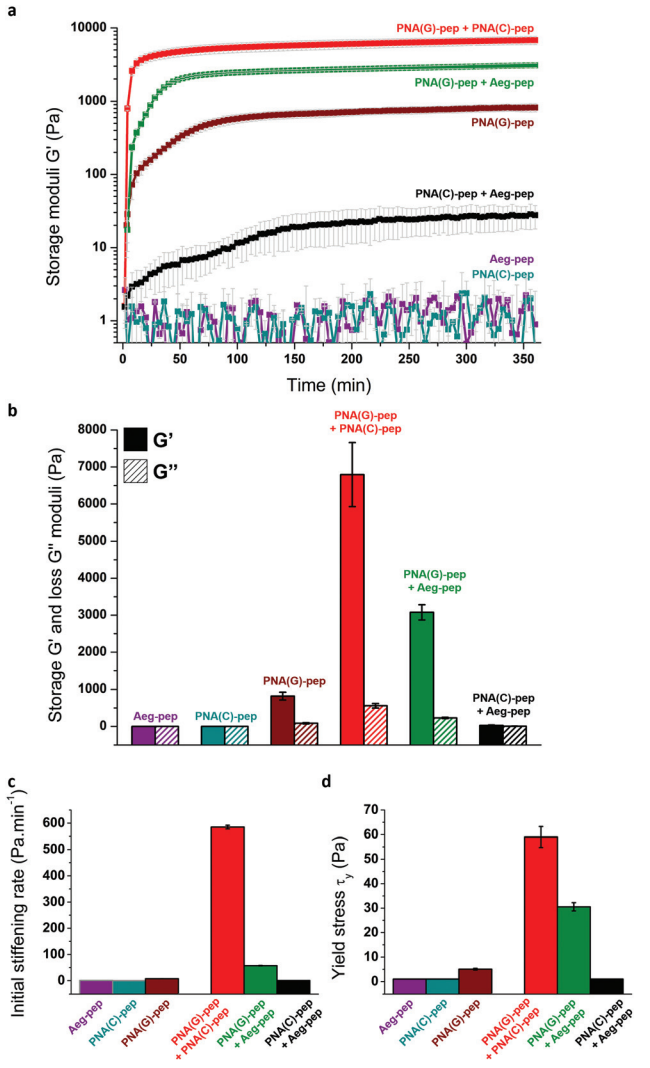

Fig. 3 (a) Time sweep rheological profiles and (b) plot of the resulting storage (G') and loss (G'') moduli after 6 hours. Plot of the characteristic (c) initial stiffening rate V_0 and (d) limiting values of the linear viscoelastic region (yield stress τ_y). All the experiments were carried out with **PNA(G)-pep**, **PNA(C)-pep** and/or **Aeg-pep** at 7.5 mM of each compound in Tris·HCl (1 M, pH 7.4).

observed for **PNA(A)-pep** + **Aeg-pep**, which exhibits the fourth highest storage modulus but the fifth initial rate. Interestingly, while all the compounds have exactly the same self-assembling heptapeptide core and only differ by the presence (or not) and the nature of the nucleobase, the presence of complementary nucleobases A + T and C + G leads to faster gelification kinetics, suggesting a cooperative effect between the nucleic acid pairs. This tendency is also observed comparing the resistance to stress characterized by the yield point τ_y corresponding to the limiting value of the linear viscoelastic region beyond which the structure of the hydrogel is destroyed. Thus, as depicted Fig. 2d and 3d (Table 1 and Fig. S7†), the stress sweep experiments (with controlled shear strain) show higher resistance to stress for **PNA(A)-pep** + **PNA(T)-pep** with τ_y = 131 Pa, better than **PNA(A)-pep** + **Aeg-pep** and **PNA-(T)-pep** + **Aeg-pep** (τ_y = 73 Pa and 26 Pa, respectively). The mixing of **PNA(G)-pep** + **PNA(C)-pep** also improves the deformation response of the resulting hydrogels (τ_y = 59 Pa), compared to the G- or the C-derivative with the nucleobase-lacking **Aeg-pep**. Once more, the collaborative effect of the complementary nucleobases is significant on the mechanical properties of the materials.

Mesoscopic scale: solvent behaviour, hydrogel scaffold and self-assembled (nano)objects

To gain further insights into the understanding of the hydrogel properties, the study of the behaviour of water which is the main constituent of the material (>98 weight%) was carried out using NMR relaxometry.[64,65] The advantages of this technique is that it does not require the addition of extra dye, nor

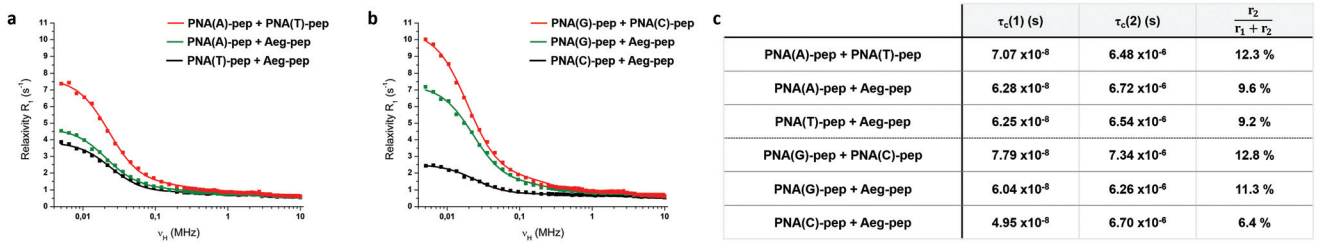

c

	$\tau_c(1)$ (s)	$\tau_c(2)$ (s)	$\frac{r_2}{r_1 + r_2}$
PNA(A)-pep + PNA(T)-pep	7.07 x10^{-8}	6.48 x10^{-6}	12.3 %
PNA(A)-pep + Aeg-pep	6.28 x10^{-8}	6.72 x10^{-6}	9.6 %
PNA(T)-pep + Aeg-pep	6.25 x10^{-8}	6.54 x10^{-6}	9.2 %
PNA(G)-pep + PNA(C)-pep	7.79 x10^{-8}	7.34 x10^{-6}	12.8 %
PNA(G)-pep + Aeg-pep	6.04 x10^{-8}	6.26 x10^{-6}	11.3 %
PNA(C)-pep + Aeg-pep	4.95 x10^{-8}	6.70 x10^{-6}	6.4 %

Fig. 4 Proton NMR dispersion profiles in which the longitudinal relaxation rate R_1 is plotted as a function of the Larmor frequency ν_H for multicomponent systems comprised of (a) **PNA(A)-pep**, **PNA(T)-pep** and/or **Aeg-pep** and (b) **PNA(G)-pep**, **PNA(C)-pep** and/or **Aeg-pep**. Continuous lines represent the best fits obtained with a sum of lorentzian functions $R_1(\nu_H) = A(0) + \sum_i \frac{A(i)}{1 + (2\pi\nu_H\tau_c(i))^2}$, where τ_c is the correlation time describing the water motion (see numeric values in (c)). The proportion of water experiencing very slow motion (last column in (c)) was obtained by comparing the weight of the lorentzians $r_i = \frac{A(i)}{\tau_c(i)}$ in each sample. (c) Table of the main characteristic values obtained from proton NMR dispersion experiments (see Table S4† for additional data).

drying or modification of the sample, allowing the study of the hydrogels prepared in strictly the same conditions as for rheological investigations. Thus, all the six blends were analysed, and the measured longitudinal relaxation times T_1 of the water protons were subsequently transformed into relaxation rates $R_1 = 1/T_1$, plotted as a function of Larmor frequency (Fig. 4a and b). To obtain quantitative data, all the dispersion curves have been deconvoluted by two Lorentzian fitting, each of them corresponding to a different kind of water population. The first one appears at low frequencies and corresponds to constrained water molecules confined in the hydrogel and in direct interaction with the nucleopeptide assemblies. These water molecules exhibit correlation time $\tau_c(2)$ spanning from 6.3 to 7.3 × 10^{-6} s (Fig. 4c), characteristic of slow movements. At higher frequencies, a second population corresponding to more free water is present for all the samples and we observe (Fig. 4c) that the hydrogel of **PNA(A)-pep** + **PNA(T)-pep**, with a correlation time $\tau_c(1)$ = 7.1 × 10^{-8} s higher than **PNA(A)-pep** + **Aeg-pep** and **PNA(T)-pep** + **Aeg-pep**, has more constrained water molecules than the two latter ones. A similar trend occurs for **PNA(G)-pep** + **PNA(C)-pep** compared to **PNA(G)-pep** or **PNA(C)-pep** in the presence of **Aeg-pep**. The results highlight the ability of the A + T and C + G systems to further constrain water molecules inside the hydrogel structure than the other mixtures. In term of water population ratio, obtained in comparing the weight of the two Lorentzians values ($r_2/(r_1 + r_2)$, Fig. 4c), the results point out the highest ratio for **PNA(G)-pep** + **PNA(C)-pep**, followed by **PNA(A)-pep** + **PNA(T)-pep**. Interestingly, all the values are in perfect accordance with the hierarchy observed in rheology: the higher the ratio (*i.e.*, the higher the proportion of constrained water molecules), the stiffer the hydrogel. Thus, we can postulate that the rigidity of a gel is function of its ability to constrain the movements of solvent's molecules. This property originates, in part, from the nature of the inherent chemical structure of the gelator and of the scaffold the peptide-assembled nanostructures form. To evaluate them, a set of SAXS experiments were carried out in strictly the same conditions than for rheology and ^{1}H NMR relaxometry. At first glance, we observe similar global shapes of the curves with, for each series (Fig. 5a and b), the highest scattering intensities $I_{max}(q)$ obtained for the mixtures containing the complementary nucleobases (in red), *i.e.*, **PNA(A)-pep** + **PNA(T)-pep** ($I_{max}(q)$ = 4.0 cm^{-1}, Fig. 5a) and **PNA(G)-pep** + **PNA (C)-pep** ($I_{max}(q)$ = 29.1 cm^{-1}, Fig. 5b). The difference of a factor of ~7 between the two systems suggests the presence of larger nanostructures for **PNA(G)-pep** + **PNA(C)-pep** than for **PNA(A)-pep** + **PNA(T)-pep**, as corroborated by the TEM images in which fibrillar assemblies of ~29 nm- and 16 nm-cross-section (Fig. 6a and b, discussed hereinafter) appear, respectively. To further exploit the data, the SAXS diffusion profiles have been fitted according to the two-correlation-length model functional form $I(q) = A/q^n + C/(1 + (qL)^m) + B$ (see Materials and methods for more details), previously reported as a relevant model for peptide-based hydrogels[66–68] and other systems.[69,70] On the one hand, the first term A/q^n describes the scattering in the

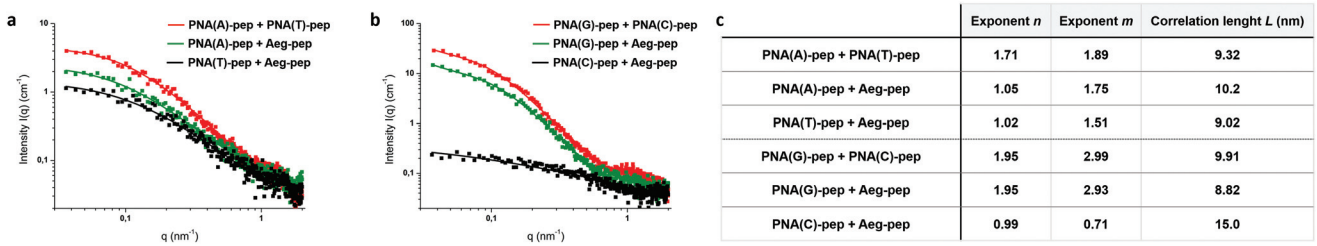

c

	Exponent *n*	Exponent *m*	Correlation lenght *L* (nm)
PNA(A)-pep + PNA(T)-pep	1.71	1.89	9.32
PNA(A)-pep + Aeg-pep	1.05	1.75	10.2
PNA(T)-pep + Aeg-pep	1.02	1.51	9.02
PNA(G)-pep + PNA(C)-pep	1.95	2.99	9.91
PNA(G)-pep + Aeg-pep	1.95	2.93	8.82
PNA(C)-pep + Aeg-pep	0.99	0.71	15.0

Fig. 5 (a and b) SAXS profiles and best fits (continuous lines, see Materials and methods for more details) obtained for all the six mixtures, and (c) table of the main characteristic values obtained from the fitting (see Table S5† for additional data).

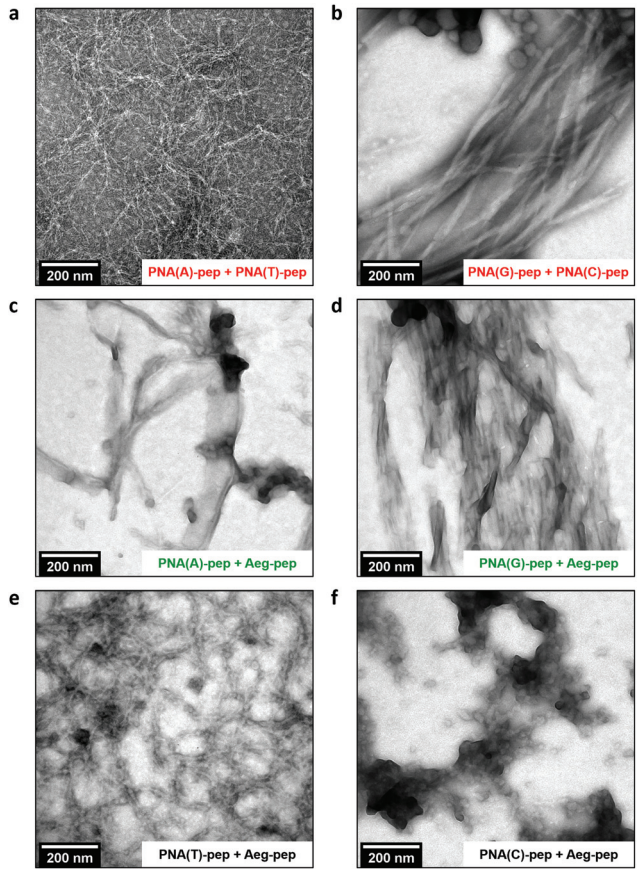

Fig. 6 TEM images of all the six multicomponent systems recorded with a magnification of ×11 500 and negative staining by phosphotungstic acid.

low-q regime and characterizes the network of the hydrogel structure at the hundred nanometer-scale. For our samples, we observe that for the mixtures **PNA(G)-pep** + **PNA(C)-pep**, **PNA(G)-pep** + **Aeg-pep** and **PNA(A)-pep** + **PNA(T)-pep** the exponents n are from 1.7 to 1.95 (Fig. 5c and Table S5†). This value range, often obtained for peptide-based assemblies,[39,66,71] reflects the scattering of Gaussian chains, consistent with previous results[66,72,73] and with TEM images in which long fibrillar structures are observed (*vide infra*). For the other samples, lower n values around ~1 are obtained, suggesting rod-like structures[68,74,75] (*i.e.*, presence of fibers) confirmed by TEM. Moreover, the n value is probably influenced for all these samples by the presence of an heterogenous population of nanostructures (*e.g.*, spherical aggregates, tape-like structures observed in TEM), as discussed hereinafter. On the other hand, the second term $C/(1 + (qL)^m)$ describes the scattering in the high-q regime and characterizes the local hydrogel network up to around ten nanometers, with the exponent m which reflects the network compactness.[66–68] The highest values are obtained for the mixtures **PNA(G)-pep** + **PNA(C)-pep**, **PNA(G)-pep** + **Aeg-pep** and **PNA(A)-pep** + **PNA(T)-pep** with m = 3.0, 2.9 and 1.9, respectively (Fig. 5c). Interestingly, we observed for our samples that the compactness is in good accordance with the hierarchy observed in rheology and in ^{1}H NMR relaxometry, *i.e.*, the stiffer the gel, the higher the ratio of constrained solvent's molecules, the more compact the peptide-based assembled network. All these results highlight the relationships between the nanostructures formed, their interactions with the solvent and the resulting mechanical properties. To support these data, a series of TEM investigations were conducted. As depicted Fig. 6a (and Fig. S9†), upon mixing the complementary **PNA(A)-pep** and **PNA(T)-pep**, a large and dense network of entangled fibers is observed, consistent with the SAXS data, with an average diameter of fibers of 6.0 ± 1.3 nm forming bundles of 16.0 ± 4.5 nm-cross-section. These data support a direct interaction, *i.e.*, a co-assembling process (and not a self-sorting one) between the two components when mixed, because alone **PNA(A)-pep** and **PNA(T)-pep** form different assemblies in terms of size and morphologies with thinner fibers with diameters of 4.9 nm and 2.5 nm, respectively.[54] By contrast to the A + T system, when the adenine derivative is in the presence of **Aeg-pep**, a more heterogeneous population of nanostructures (as suspected based on the SAXS profiles, *vide supra*) appears, including few fibers (9.1 ± 1.4 nm of diameter) and two-dimensional sheet structures (*i.e.*, ribbons) from 20 nm to more than 800 nm-width (Fig. 6c and Fig. S9†). The sample **PNA(T)-pep** + **Aeg-pep** also exhibits the formation of both fibers and, mainly, tape-like structures of varying sizes. In parallel, the blend of **PNA(G)-pep** and **PNA(C)-pep** leads to long (>500 nm) and large (28.7 ± 7.8 nm-cross-section) fibers (consistent with the SAXS data), contrasting with the already reported structures adopted by each compound alone in which thinner fibers were observed (diameter <5.1 nm).[54] These differences are in favour of a co-assembling process between the two complementary nucleopeptides, such as the A + T derivative mixing. Interestingly, we can also notice that the stiffer hydrogels possess fiber-like nanostructures (*i.e.*, **PNA(A)-pep** + **PNA(T)-pep**, **PNA(G)-pep** + **PNA(C)-pep**), while in the weaker ones heterogeneous and two-dimensional nanoobjects are formed. This is confirmed by the study of the TEM images of **PNA(G)-pep** or **PNA(C)-pep** in the presence of **Aeg-pep** which assemble into long and thin (*i.e.*, 14.2 ± 3.3 nm-cross-section) ribbons or ill-defined spherical aggregates (around 20–30 nm), respectively. The latter fail to form an efficient hydrogel scaffold and consequently leads to the weakest mechanical properties among all the six multicomponent materials (*vide supra*).

Molecular and supramolecular scales: secondary structures and intermolecular interactions

The morphological data can be compared to structural data obtained by circular dichroism (CD) and Fourier-transform infrared (FTIR). Concerning the latter method, for all the six mixtures, the presence of a main band centred at 1619–1622 cm^{-1} along with a second band in the 1690–1693 cm^{-1} region (Fig. S10†) is clearly indicative of anti-parallel β-sheet structures,[76] typical of peptide assemblies forming hydrogels.[1,2] Comparing the measured absorbance of the mixtures with the arithmetic mean of each constituting

compound, we can state that the compounds are co-assembled (and not self-sorted, see Fig. S10†).[21] A similar approach was applied using CD, and the dichroic spectra of all the mixtures (Fig. S11†) show characteristic β-sheet negative bands around 215–220 nm (corresponding to n–π* electronic transitions of the amide groups,[77] which are slightly red-shifted (up to 230 nm) for **PNA(A)-pep** + **PNA(T)-pep** and **PNA(T)-pep** + **Aeg-pep**, suggesting more twisted β-sheet structures[78,79]) and a positive band at 186–188 nm (π–π* electronic transitions of the amides). Additionally, a distinctive minimum at 200 nm is observed for all the mixtures due to aromatic interactions between phenylalanine moieties (π–π* electronic transitions[80]). The comparison between the measured spectra and the arithmetic mean of the spectra of each constituent reveals clear differences excluding a self-sorting assembly and supporting once more a co-assembling process.[21]

The presence of π-stacking interactions involving phenylalanine moieties is also confirmed by fluorescence spectroscopy (Fig. 7 and Fig. S12†) which reveals a main emission peak centred in the 400–420 nm range originating from an excitation between 345 and 351 nm (*i.e.*, Stokes shifts = 0.57 to 0.65 eV). This fluorescence, observable for all the six multicomponent hydrogels, can be attributed to the exciton exchange between phenylalanine rings in intermolecular interactions.[81,82] At lower wavelength, an additional excitation peak appears in the 306–315 nm range (depending on the multicomponent system considered, with Stokes shifts = 0.84–1.05 eV), characteristic of stacking associations of nucleic acids in water.[54,83] These data highlight the stacking interactions between phenylalanine moieties but also between nucleobases

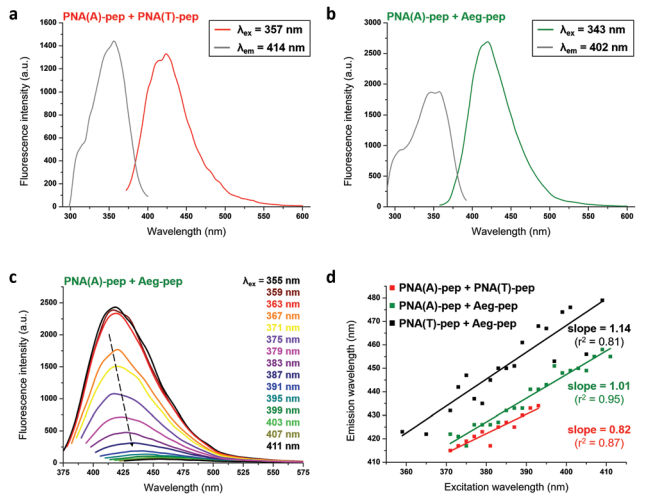

Fig. 7 Selected fluorescence emission and excitation spectra for (a) the **PNA(A)-pep** + **PNA(T)-pep** and (b) **PNA(A)-pep** + **Aeg-pep** multicomponent systems (see Fig. S12† for the other mixtures) (c) Evolution of the fluorescence emission spectra at different excitation wavelengths for **PNA(A)-pep** + **Aeg-pep** multicomponent systems (see Fig. S13† for the other mixtures) and (d) plot of the linear correlation between emission and excitation wavelengths exhibiting a red-edge excitation shift (REES), and corresponding regression slope and r^2 values for multicomponent systems comprised of **PNA(A)-pep**, **PNA(T)-pep** and/or **Aeg-pep**.

in the co-assembly processes. Due to the constrained environment in which the fluorophores (*i.e.*, nucleobase, phenylalanine) are in the gel state, a red-edge excitation shift (REES) phenomenon occurs (Fig. 7c, d and Fig. S13†). Interestingly, the presence of **Aeg-pep** and pyrimidine derivatives (*i.e.*, thymine and cytosine derivatives) improves the REES effect with, on the one hand **PNA(T)-pep** + **Aeg-pep** > **PNA(A)-pep** + **Aeg-pep** > **PNA(A)-pep** + **PNA(T)-pep** and, on the other hand **PNA(C)-pep** + **Aeg-pep** > **PNA(G)-pep** + **Aeg-pep** > **PNA(G)-pep** + **PNA(C)-pep**. These results can be correlated with the higher **PNA(T)-pep** + **Aeg-pep** and **PNA(C)-pep** + **Aeg-pep** propensities to interact *via* π-stacking interactions, as observed in their CD signatures with an exacerbated Cotton effect at ~200 nm (*vide supra*, Fig. S11†), corresponding to more aromatic interactions between phenylalanine moieties compared to the other mixtures.

To gain further information about the self-assembly process in a kinetic point of view, we harnessed their β-sheet structuration to perform Thioflavin T fluorescence experiments. Indeed, widely reported for the detection and analysis of amyloid fibrils both for research and diagnosis in a context of neurodegenerative disease such as Parkinson's, Alzheimer's or Prion's diseases, Thioflavin T (ThT) is a non-fluorescent compound when free in solution becoming fluorescent upon binding to β-sheets (a minimum of three to four stacked β-sheets are required for the ThT binding).[84,85] Thus, the evolution of the ThT fluorescence was recorded as a function of time for all the studied mixtures and plotted Fig. 8a and b. From these data, three main values have been extracted: the maximum fluorescence intensity I_{max} indicative of the fibrils numbers and morphologies, the lag time t_{lag} corresponding to the end of the non-fluorescent initial state in which starting monomers undergo primary nucleation,[86] and the apparent rate constant k_{app}, defined as the growth rate of fibrils elongation (Fig. 8c). On the one hand, the **PNA(A)-pep** + **PNA(T)-pep** mixture, in which the two complementary nucleobases are present, exhibits a higher I_{max} value (28%) than the two controls **PNA(A)-pep** + **Aeg-pep** and **PNA(T)-pep** + **Aeg-pep** with I_{max} = 7.5% and 2.6%, respectively. Moreover, while these three systems have no measurable lag times (t_{lag} <1 min), the constant rates are different with a faster elongation rate for **PNA(A)-pep** + **PNA(T)-pep** (k_{app} = 25.6 h^{-1}) than for each nucleobase-containing component in the presence of **Aeg-pep**. These results are in perfect accordance with the hierarchy observed in rheology in terms of macroscopic mechanical properties and kinetics, and with ^{1}H NMR relaxometry and SAXS experiments (*vide supra*). On the other hand, the **PNA(G)-pep** + **PNA(C)-pep** mix also exhibits the highest intensity with I_{max} = 37% compared to **PNA(G)-pep** or **PNA(C)-pep** in the presence of **Aeg-pep**, with I_{max} = 21% and <1%, respectively. For **PNA(C)-pep**, the absence of fluorescence can be linked to its inability to form a self-supporting hydrogel and to self-assemble mainly into ill-defined morphologies, as observed in TEM and FTIR (*vide supra*). Interestingly, in a kinetic point of view, the **PNA(G)-pep** + **PNA(C)-pep** blend has a longer t_{lag} and a shorter k_{app} (*i.e.*, a slower kinetic of formation) than

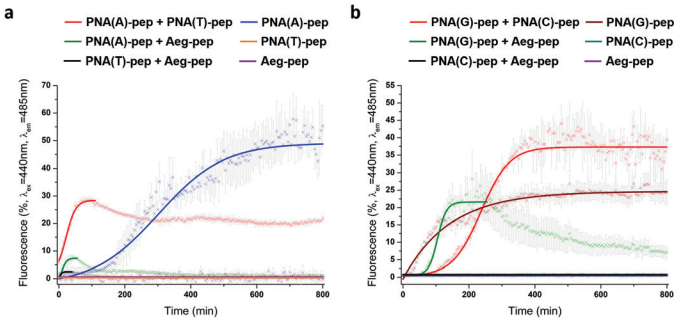

c

	Maximum intensity (a.u.)	Lag time (min)	k_{app} (h^{-1})
PNA(A)-pep + PNA(T)-pep	**28.3** (dev. std. 1.3)	**< 1**	**25.6** (dev. std. 1.1)
PNA(A)-pep + Aeg-pep	**7.49** (dev. std. 0.85)	**< 1**	**19.8** (dev. std. 1.5)
PNA(T)-pep + Aeg-pep	**2.56** (dev. std. 0.37)	**< 1**	**7.44** (dev. std. 1.54)
PNA(G)-pep + PNA(C)-pep	**37.3** (dev. std. 4.2)	**143.9** (dev. std. 8.1)	**12.7** (dev. std. 1.2)
PNA(G)-pep + Aeg-pep	**21.6** (dev. std. 4.0)	**76.0** (dev. std. 3.0)	**22.8** (dev. std. 1.5)
PNA(C)-pep + Aeg-pep	**0.78** (dev. std. 0.06)	*n.d.*	*n.d.*

Fig. 8 (a and b) Fibrils formation monitored by Thioflavin T fluorescence assay (λ_{ex} = 440 nm, λ_{em} = 485 nm) as a function of time for samples comprised of (a) **PNA(A)-pep**, **PNA(T)-pep** and/or **Aeg-pep** (in Tris·HCl (1 M, pH 7.4), at 5 mM of each compound) and (b) **PNA(G)-pep**, **PNA(C)-pep** and/or **Aeg-pep** (in Tris·HCl (1 M, pH 7.4), at 2.5 mM of each compound). (c) Characteristic maximum intensities, lag time (t_{lag}) and apparent rate constants (k_{app}) reported for all the equimolar multicomponent mixtures (see Table S6† for additional data).

PNA(G)-pep + **Aeg-pep** (Fig. 8c), whereas its macroscopic initial rate (V_0 = 585 Pa min^{-1}, Table 1) determined using rheology is faster than the latter one (V_0 = 57 Pa min^{-1}). These data can be explained based on the TEM images: while **PNA(G)-pep** + **PNA(C)-pep** co-assemble into well-defined long and large fibers (*vide supra*), the **PNA(G)-pep** + **Aeg-pep** mix forms long and thin ribbons which constitute a weaker hydrogel backbone leading consequently to weaker mechanical properties (lower storage modulus G′ and lower population of constrained water in ^{1}H NMR relaxometry, *vide supra*), as already reported.[87,88]

Conclusions

Through a comprehensive multiscale analysis approach, we have evaluated and decipher the physicochemical and mechanical properties of a series of multicomponent peptide-based hydrogels formulated from a mixture of hybrid DNA-nucleobase-containing peptide derivatives. Our work demonstrates that, starting from five different compounds, the choice of the blend (*nota*: six are considered herein) drastically impacts both the assembly processes and the resulting structural, physicochemical and mechanical hydrogel properties, from the molecular to the microscopic, mesoscopic and, finally, macroscopic scales. As discussed throughout this article, these macroscopic aspects originate from differences at lower scales and are correlated with the morphologies of nanoobjects the co-assemblies form, the compactness of the hydrogel scaffolds the latter build, and their resulting abilities to constrain solvent's molecules inside the soft materials. Thus, depending on the prepared mixture, a wide range of mechanical properties has been obtained with stiffnesses spanning from 30 Pa to 6800 Pa (storage modulus G'), resistances to stress from less than 1 Pa to 131 Pa and sol/gel transition times $t_{s/g}$ from less than 2 min to more than 4 days. Interestingly, the stiffest and fastest hydrogels were obtained for the two multicomponent mixtures containing the two complementary DNA-nucleobases (*i.e.*, adenine + thymine and guanine + cytosine)-peptide-based derivatives. For the other mixtures containing Aeg-pep, their mechanical and kinetic properties seem to be driven by the PNA(X)-pep (X = A, T, C, G): indeed, their storage moduli, sol/gel transition time $t_{s/g}$, resistance to stress (τ_y), compactness, or ability to constrain the solvent, follow the same trend as for the hydrogels formulated from PNA(X)-pep alone, *i.e.*, G- > A- > T- > C-containing nucleopeptide, as previously reported.[54] This can be explained, *inter alia*, by the better ability of the purines G and A to interact *via* π-stacking, compared to the pyrimidines C and T.

The results reported herein confirm the interest of such multicomponent systems and outline the complexity of studying and understanding such complex supramolecular assemblies.[15,16,20,21,40] For these reasons, we assume that this challenging research area requires a systematic multiscale approach to rationalize the role and the impact of each constituent of the blend. Indeed, with virtually unlimited possibilities in terms of peptide derivatives design (*e.g.*, number and nature of the amino acids, sequence, chemical modification brought), number of constituents (*nota*: two have been chosen herein) or equivalent ratio between each constituent, the multicomponent physical hydrogels open new horizons in terms of applications with a more precise control of the physicochemical and mechanical properties, allowing chemists and biologists to fine tune the hydrogel features for specific and precise needs.[15,20,89,90] It is safe to bet that, following the reign of monocomponent peptide-based hydrogels, multicomponent peptide-based hydrogels will bring new molecular tools to widen the scope of possibilities and will become the new standards.

Materials and methods

Peptide synthesis and purification

Peptides were synthesized at a 400 μmol-scale both manually and on an automated ResPep XL synthesizer following an already reported protocol[54] (see ESI† for a brief description of the protocol).

Sample preparation

As a global procedure, the samples were prepared at 7.5 mM of each peptide derivative (*i.e.*, a total concentration of 15 mM for

the 1 : 1 mixtures) by dissolving each sample in Tris·HCl (1 M, pH 7.4) or in a NaF aqueous solution (0.67 M, pH 7.4) for CD experiments. All the buffers were prepared in deionized water (18.2 MΩ cm). As a standard procedure, the glass vials containing the solutions were sealed and subsequently heated (heatgun, 5 min, 70 °C), allowing a complete dissolution of the starting powder. Samples were used directly (rheology and Thioflavin T fluorescence experiments) or stored 24 hours at room temperature before analysis.

Rheological characterizations

Dynamic rheological measurements were performed on an AR2000 rheometer (TA Instruments) operating in oscillatory mode, equipped with a Peltier plate temperature control and a Couette geometry immersed inside the samples. All the measurements were repeated a minimum of three times. Time sweep experiments were carried out at constant shearing strain using a 0.5% strain amplitude and a 1 rad s^{-1} angular frequency during 360 min, 20 °C. The apparent rate constant k_{app} was calculated from the slot of $G' = f(t)$ in the very first five minutes. Frequency sweep experiments were conducted at constant shearing strain using a 0.5% strain amplitude for a range of 0.1–100 rad s^{-1}, at 20 °C. Stress sweep experiments were performed for a range of 0.46–1000 Pa applied stress at a 1 rad s^{-1} angular frequency, 20 °C. The limiting values of the linear viscoelastic region (*i.e.*, the yield point τ_y) correspond to the stress value at which the storage modulus loses 10% of its maximal value. Thermal recovery experiments were conducted at constant shearing strain using a 0.5% strain amplitude, a 1 rad s^{-1} angular frequency applying five heating/cooling cycles. During each cycle, after a one-hour stabilization step at 20 °C, the samples were heated up at 10 °C min^{-1} to reach 85 °C, followed by a 5 min stabilization time (in which no shear was applied). Then, samples were cooled down at 5 °C min^{-1} to reach 20 °C. The storage (G') and loss (G'') moduli reported were chosen at the end of each stabilization step.

Relaxometry

The ^{1}H NMR relaxometry experiments were performed in a 5 kHz–10 MHz Larmor frequency range with a Stelar SMARTracer fast-field-cycling relaxometer (Stelar company). Samples were conditioned in 5 mm NMR tubes and measurements were done at 25 °C. 32 different values of the static magnetic field were sampled, with a fixed acquisition field of 7.2 MHz (^{1}H Larmor frequency). Eight accumulations and a recycle delay of 8 s were used for all measurements. Pre-polarized measurements were done below 4 MHz with a polarization duration of 1.5 s. Field-switching time was 3 ms. For each B_0 value, R_1 were obtained from the magnetization monoexponential evolution as a function of the time, sampled with 16 values between 0.01 and 4 times the longitudinal relaxation time.

Small-angle X-ray scattering (SAXS)

Small-angle X-Ray scattering (SAXS) measurements were carried out on a SAXSpace instrument (Anton Paar), using line-collimation system at the SAXS facility in the "Institut Jean Barriol". This instrument is attached to an ID 3003 laboratory X-Ray generator (General Electric) equipped with a sealed X-Ray tube (PANalytical, $\lambda_{Cu,\ K\alpha}$ = 0.1542 nm) operating at 40 kV and 50 mA. After the solubilization step, the samples were introduced in a "Special Glass" capillary (2.0 mm-diameter), subsequently sealed and let to gel for 24 hours before being placed at 25 °C, inside an evacuated sample chamber equipped with a temperature-controlled sample holder unit, and exposed to X-Ray beam for about 50 min. Scattering of X-Ray beam was recorded by a 1D detector (Mythen 2 with strip of 50 μm × 8 mm) placed at 250 mm distance from sample. Scattering intensities $I(q)$ were provided as a function of the magnitude of the scattering vector $q = (4\pi/\lambda)\sin(\theta)$, where 2θ is the total scattering angle. Thanks to a translucent beamstop allowing the measurement of an attenuated primary beam at $q = 0$, all measured intensities can be calibrated by normalizing the attenuated primary intensity. The data were collected in a q-range from 0.03 to 7 nm^{-1} and then corrected for the background scattering, from the empty capillary and the solvent (Tris·HCl (1 M, pH 7.4)), and for slit-smearing effects by a desmearing procedure, using Lake method. After correction, obtained intensities are scaled into absolute units using water as a reference material. The SAXS data were analyzed and fitted with the SasView 4.1 software, using the *CorrLength* model corresponding to the functional form:

$$I(q) = \frac{A}{q^n} + \frac{C}{1 + (qL)^m} + B$$

in which $I(q)$ is the scattering intensity, q is the scattering vector, A, B and C are constants, L is the correlation length, n and m are the scaling exponents at low and high q, respectively.[68]

Transmission electron microscopy

Transmission Electron Microscopy (TEM) experiments were performed on a Philips CM200 electron microscope operating at 200 kV and fitted with CCD MSC 600 Gatan camera. Samples were prepared by placing a drop of each sample (1.5 mM in 100 mM Tris·HCl, pH 7.4) on 200-mesh carbon-coated copper grids (CF-200-Cu-50) for 3 min. The excess fluid was subsequently removed and a drop of phosphotungstic contrasting agent (2% w/w in deionized water) was deposited for 1 min. The excess was subsequently removed and the grid was air-dried for 5 min before analysis. Collected data were analysed using Gatan DigitalMicrograph and Fiji software.

FTIR

FTIR measurements were carried out at room temperature on a Tensor27 spectrometer (Bruker) set to ATR mode, in a range of 4000–900 cm^{-1} with a 2 cm^{-1}-resolution. Infrared spectra represent an average of 256 scans recorded in a single-beam mode and corrected for the background. For the calculation of the arithmetic means, the FTIR signals of each peptide alone at 15 mM[54] were added and divided by two. Data were analyzed, smoothed (Savitzky–Golay, 2nd order, 9 points), and treated using the OPUS software.

Circular dichroism

Circular dichroism spectra were recorded using a Chirascan Plus spectrophotometer (Applied Photophysics) at 20 °C. Hydrogels were prepared in an aqueous solution of NaF (667 mM in deionized water (18.2 MΩ cm) adjusted to pH = 7.4 with NaOH) at a final concentration of peptide of 10 mM. The samples were deposited carefully inside a 0.01 nm-pathlength dismountable cuvette prior to be analyzed. Their spectra were measured between 180–320 nm (step = 0.5 nm, response = 0.5 s, bandwidth = 1 nm) averaged on three repetitions. After background subtraction and smoothing (Savitzky–Golay, 2nd order, 9 points), all raw data (θ, mdeg) were converted into mean residual ellipticity (MRE) according to the equation below:

$$\mathrm{MRE} = \frac{\theta}{(n-1) \times c \times d \times 10}$$

where MRE is in ° cm^2 $dmol^{-1}$, d is the cuvette pathlength in cm, and c the molar concentration in mol L^{-1}. For the calculation of the arithmetic means, the MRE of each peptide alone at 10 mM (ref. 54) were added and divided by two.

Fluorescence

Fluorescence spectra were recorded using a FP-8300 spectrofluorometer (JASCO Corp.) on 5 mM samples in Tris·HCl buffer (1 M, pH 7.4). For each experiment 700 μL of the samples were transferred into quartz cuvettes (1 cm-pathlength). Fluorescence spectra were obtained at 20 °C with a 3D measurements mode (parameters: scanning speed = 200 nm min^{-1}, response time = 1 s, emission bandwidth = 5 nm and excitation bandwidth = 1 nm). Excitation spectra were recorded from 290 to 420 nm (step = 1 nm) for an emission wavelength varying from 302 to 580 nm (step = 2 nm), and emission spectra were recorded from 300 nm to 600 nm (step = 1 nm) for an excitation wavelength varying from 290 to 420 nm (step = 2 nm). Data were processed and smoothed (Savitzky–Golay, 2nd order, 9 points) using OriginPro 8.5. For the determination of the REES phenomenon, the maximum of emission is spotted on each smoothed emission spectrum for all compounds as a function of the excitation wavelength. Subsequently, the graph $\lambda_{em} = f(\lambda_{ex})$ was plotted and fitted by a linear regression on concerned points.

Thioflavin T fluorescence

Stock solutions of Thioflavin T (750 μM) were prepared in deionized water (18.2 MΩ cm), and the actual concentration was determined through UV-vis spectral analysis at 412 nm with the molar extinction coefficient $\varepsilon_{412\ nm}$ = 36 000 M^{-1} cm^{-1}.[84] Samples were prepared mixing the ThT solution with peptide solutions (previously dissolved in Tris ·HCl (1 M, pH 7.4)) to reach final concentrations [ThT] = 100 μM and concentration of each peptide = 2.5 mM (for **PNA(C)-pep**, **PNA(G)-pep** and **Aeg-pep** mixtures, Fig. 8b and c) or 5 mM (for **PNA(A)-pep**, **PNA(T)-pep** and **Aeg-pep** mixtures, Fig. 8a and c). *Note*: Two different sets of concentration were chosen to obtain exploitable signals in less than 15 hours. Samples were subsequently transferred into black 96-well microplates (150 μL per well), protected with an optical adhesive film (to avoid evaporation) and the fluorescence was measured during 1000 min (λ_{ex} = 440 nm, λ_{em} = 485 nm, response = 1 s, excitation/emission bandwidth = 6 nm, sensitivity PMT = 800 V, temperature = 25 °C, 1 point each 5 minutes, orbital shacking (3 mm, 5 Hz)) with a Xenius SAFAS. Fluorescence emission at 485 nm was plotted as a function of time, and results are mean of three to four experiments. Data were fitted using a sigmoidal growth model,[86] and characteristic values were extracted from the graphs: the lag time t_{lag} and t_{50} corresponding to the time required to reach 5% and 50% of the maximum fluorescence intensity, respectively, and the apparent growth rate k_{app} calculated from the tangent at the inflexion point t_{50}.

Conflicts of interest

There are no conflicts to declare.

Acknowledgements

L. S and M.-C. A.-P. acknowledge the Centre National de la Recherche Scientifique (CNRS) for funding. L. S. thanks the Agence National de la Recherche (ANR-20-CE06-0010-01 MUNCH) for funding. T. G. thanks the Ministère de l'Enseignement Supérieur, de la Recherche et de l'Innovation (MESRI) for his Ph.D. grant. The authors acknowledge Mathilde Achard for support on peptide synthesis and purification, and Anne Robert, Dr Sylvie Fournel-Gigleux and Dr Sandrine Gulberti for allowing access to the Xenius SAFAS fluorimeter.

References

1 A. Dasgupta, J. H. Mondal and D. Das, *RSC Adv.*, 2013, **3**, 9117–9149.
2 L. M. De Leon Rodriguez, Y. Hemar, J. Cornish and M. A. Brimble, *Chem. Soc. Rev.*, 2016, **45**, 4797–4824.
3 W. Y. Seow and C. A. E. Hauser, *Mater. Today*, 2014, **17**, 381–388.
4 D. Seliktar, *Science*, 2012, **336**, 1124–1128.
5 X. Q. Dou and C. L. Feng, *Adv. Mater.*, 2017, **29**, 1604062.
6 J. Li, R. Xing, S. Bai and X. Yan, *Soft Matter*, 2019, **15**, 1704–1715.
7 K. Sato, M. P. Hendricks, L. C. Palmer and S. I. Stupp, *Chem. Soc. Rev.*, 2018, **47**, 7539–7551.
8 L. Stefan, in *Amino Acid – New Insights and Roles in Plant and Animal*, ed. T. Asao and M. Asaduzzaman, IntechOpen, 2017, pp. 31–73.
9 X. Du, J. Zhou, J. Shi and B. Xu, *Chem. Rev.*, 2015, **115**, 13165–13307.
10 S. Fleming and R. V. Ulijn, *Chem. Soc. Rev.*, 2014, **43**, 8150–8177.

11 A. Bertolani, L. Pirrie, L. Stefan, N. Houbenov, J. S. Haataja, L. Catalano, G. Terraneo, G. Giancane, L. Valli, R. Milani, O. Ikkala, G. Resnati and P. Metrangolo, *Nat. Commun.*, 2015, **6**, 7574.
12 M. M. Nguyen, K. M. Eckes and L. J. Suggs, *Soft Matter*, 2014, **10**, 2693–2702.
13 A. Rajbhandary and B. L. Nilsson, *Pept. Sci.*, 2017, **108**, e22994.
14 M. I. A. Ibrahim, G. Pickaert, L. Stefan, B. Jamart-Grégoire, J. Bodiguel and M. C. Averlant-Petit, *RSC Adv.*, 2020, **10**, 43859–43869.
15 B. O. Okesola and A. Mata, *Chem. Soc. Rev.*, 2018, **47**, 3721–3736.
16 D. M. Raymond and B. L. Nilsson, *Chem. Soc. Rev.*, 2018, **47**, 3659–3720.
17 L. Yu, K. Dean and L. Li, *Prog. Polym. Sci.*, 2006, **31**, 576–602.
18 C. Koning, M. Van Duin, C. Pagnoulle and R. Jerome, *Prog. Polym. Sci.*, 1998, **23**, 707–757.
19 L. Feng, K. Y. Wang, G. S. Day and H. C. Zhou, *Chem. Soc. Rev.*, 2019, **48**, 4823–4853.
20 P. Makam and E. Gazit, *Chem. Soc. Rev.*, 2018, **47**, 3406–3420.
21 E. R. Draper and D. J. Adams, *Chem. Soc. Rev.*, 2018, **47**, 3395–3405.
22 A. Tajima, W. Liu, I. Pradhan, S. Bertera, C. Bagia, M. Trucco, W. S. Meng and Y. Fan, *Clin. Immunol.*, 2015, **160**, 82–89.
23 X. Liu, X. Wang, A. Horii, X. Wang, L. Qiao, S. Zhang and F. Z. Cui, *Nanoscale*, 2012, **4**, 2720–2727.
24 T. Y. Cheng, M. H. Chen, W. H. Chang, M. Y. Huang and T. W. Wang, *Biomaterials*, 2013, **34**, 2005–2016.
25 D. Cigognini, A. Satta, B. Colleoni, D. Silva, M. Donegà, S. Antonini and F. Gelain, *PLoS One*, 2011, **6**, e19782.
26 S. Boothroyd, A. Saiani and A. F. Miller, *Biopolymers*, 2014, **101**, 669–680.
27 A. Scelsi, B. Bochicchio, A. Smith, V. L. Workman, L. A. Castillo Diaz, A. Saiani and A. Pepe, *J. Biomed. Mater. Res., Part A*, 2019, **107**, 535–544.
28 C. Diaferia, G. Morelli and A. Accardo, *J. Mater. Chem. B*, 2019, **7**, 5142–5155.
29 C. Diaferia, M. Ghosh, T. Sibillano, E. Gallo, M. Stornaiuolo, C. Giannini, G. Morelli, L. Adler-Abramovich and A. Accardo, *Soft Matter*, 2019, **15**, 487–496.
30 S. M. Hsu, F. Y. Wu, T. S. Lai, Y. C. Lin and H. C. Lin, *RSC Adv.*, 2015, **5**, 22943–22946.
31 E. Y. Du, F. Ziaee, L. Wang, R. E. Nordon and P. Thordarson, *Polym. J.*, 2020, **52**, 947–957.
32 M. Halperin-Sternfeld, M. Ghosh, R. Sevostianov, I. Grigoriants and L. Adler-Abramovich, *Chem. Commun.*, 2017, **53**, 9586–9589.
33 E. V. Alakpa, V. Jayawarna, A. Lampel, K. V. Burgess, C. C. West, S. C. J. Bakker, S. Roy, N. Javid, S. Fleming, D. A. Lamprou, J. Yang, A. Miller, A. J. Urquhart, P. W. J. M. Frederix, N. T. Hunt, B. Péault, R. V. Ulijn and M. J. Dalby, *Chem*, 2016, **1**, 298–319.
34 K. J. Nagy, M. C. Giano, A. Jin, D. J. Pochan and J. P. Schneider, *J. Am. Chem. Soc.*, 2011, **133**, 14975–14977.
35 R. J. Swanekamp, J. J. Welch and B. L. Nilsson, *Chem. Commun.*, 2014, **50**, 10133–10136.
36 G. Cinar, H. Ceylan, M. Urel, T. S. Erkal, E. Deniz Tekin, A. B. Tekinay, A. Dâna and M. O. Guler, *Biomacromolecules*, 2012, **13**, 3377–3387.
37 J. K. Sahoo, M. A. Vandenberg, E. E. Ruiz Bello, C. D. Nazareth and M. J. Webber, *Nanoscale*, 2019, **11**, 16534–16543.
38 M. Tena-Solsona, S. Alonso-De Castro, J. F. Miravet and B. Escuder, *J. Mater. Chem. B*, 2014, **2**, 6192–6197.
39 P. J. S. King, M. G. Lizio, A. Booth, R. F. Collins, J. E. Gough, A. F. Miller and S. J. Webb, *Soft Matter*, 2016, **12**, 1915–1923.
40 J. Raeburn and D. J. Adams, *Chem. Commun.*, 2015, **51**, 5170–5180.
41 Y. M. Abul-Haija, G. G. Scott, J. K. Sahoo, T. Tuttle and R. V. Ulijn, *Chem. Commun.*, 2017, **53**, 9562–9565.
42 C. K. Thota, A. A. Berger, L. Elomaa, C. Nie, C. Böttcher and B. Koksch, *ACS Omega*, 2020, **5**, 8557–8563.
43 T. Macculloch, A. Buchberger and N. Stephanopoulos, *Org. Biomol. Chem.*, 2019, **17**, 1668–1682.
44 X. Li, Y. Kuang, H. C. Lin, Y. Gao, J. Shi and B. Xu, *Angew. Chem., Int. Ed.*, 2011, **50**, 9365–9369.
45 D. Yuan, X. Du, J. Shi, N. Zhou, J. Zhou and B. Xu, *Angew. Chem., Int. Ed.*, 2015, **54**, 5705–5708.
46 D. Yuan, X. Du, J. Shi, N. Zhou, A. A. Baoum, K. O. Al Footy, K. O. Badahdah and B. Xu, *Beilstein J. Org. Chem.*, 2015, **11**, 1352–1359.
47 K. Baek, A. D. Noblett, P. Ren and L. J. Suggs, *ACS Appl. Bio Mater.*, 2019, **2**, 2812–2821.
48 J. T. M. DiMaio, T. M. Doran, D. M. Ryan, D. M. Raymond and B. L. Nilsson, *Biomacromolecules*, 2017, **18**, 3591–3599.
49 R. Freeman, M. Han, Z. Álvarez, J. A. Lewis, J. R. Wester, N. Stephanopoulos, M. T. McClendon, C. Lynsky, J. M. Godbe, H. Sangji, E. Luijten and S. I. Stupp, *Science*, 2018, **362**, 808–813.
50 A. Mohammed, A. F. Miller and A. Saiani, *Macromol. Symp.*, 2007, **251**, 88–95.
51 J. Gao, C. Tang, M. A. Elsawy, A. M. Smith, A. F. Miller and A. Saiani, *Biomacromolecules*, 2017, **18**, 826–834.
52 E. Quijano, R. Bahal, A. Ricciardi, W. M. Saltzman and P. M. Glazer, *Yale J. Biol. Med.*, 2017, **90**, 583–598.
53 D. Bonifazi, L. E. Carloni, V. Corvaglia and A. Delforge, *Artif. DNA PNA XNA*, 2012, **3**, 112–122.
54 T. Giraud, S. Bouguet-Bonnet, P. Marchal, G. Pickaert, M.-C. Averlant-Petit and L. Stefan, *Nanoscale*, 2020, **12**, 19905–19917.
55 M. C. Cringoli, S. Kralj, M. Kurbasic, M. Urban and S. Marchesan, *Beilstein J. Nanotechnol.*, 2017, **8**, 1553–1562.
56 J. Rubio-Magnieto, M. Tena-Solsona, B. Escuder and M. Surin, *RSC Adv.*, 2017, **7**, 9562–9566.
57 S. H. Hiew, H. Mohanram, L. Ning, J. Guo, A. Sánchez-Ferrer, X. Shi, K. Pervushin, Y. Mu, R. Mezzenga and A. Miserez, *Adv. Sci.*, 2019, **6**, 1901173.

58 H. Arakawa, K. Takeda, S. L. Higashi, A. Shibata, Y. Kitamura and M. Ikeda, *Polym. J.*, 2020, **52**, 923–930.
59 W. Liyanage and B. L. Nilsson, *Langmuir*, 2016, **32**, 787–799.
60 R. Jain and S. Roy, *RSC Adv.*, 2019, **9**, 38745–38759.
61 M. C. Branco, F. Nettesheim, D. J. Pochan, J. P. Schneider and N. J. Wagner, *Biomacromolecules*, 2009, **10**, 1374–1380.
62 A. Z. Cardoso, A. E. A. Alvarez, B. N. Cattoz, P. C. Griffiths, S. M. King, W. J. Frith and D. J. Adams, *Faraday Discuss.*, 2013, **166**, 101–116.
63 D. M. Ryan, S. B. Anderson and B. L. Nilsson, *Soft Matter*, 2010, **6**, 3220–3231.
64 R. Kimmich and E. Anoardo, *Prog. Nucl. Magn. Reson. Spectrosc.*, 2004, **44**, 257–320.
65 R. Kimmich, in *NMR – Tomography, Diffusometry, Relaxometry*, ed. R. Kimmich, Springer, 1st edn, 1997.
66 R. A. Hule, R. P. Nagarkar, B. Hammouda, J. P. Schneider and D. J. Pochan, *Macromolecules*, 2009, **42**, 7137–7145.
67 R. A. Hule, R. P. Nagarkar, A. Altunbas, H. R. Ramay, M. C. Branco, J. P. Schneider and D. J. Pochan, *Faraday Discuss.*, 2008, **139**, 251–264.
68 J. B. Guilbaud and A. Saiani, *Chem. Soc. Rev.*, 2011, **40**, 1200–1210.
69 B. Hammouda, F. Horkay and M. L. Becker, *Macromolecules*, 2005, **38**, 2019–2021.
70 B. Hammouda, D. L. Ho and S. Kline, *Macromolecules*, 2004, **37**, 6932–6937.
71 E. R. Da Silva, W. A. Alves, V. Castelletto, M. Reza, J. Ruokolainen, R. Hussain and I. W. Hamley, *Chem. Commun.*, 2015, **51**, 11634–11637.
72 S. Ramachandran, J. Trewhella, Y. Tseng and Y. B. Yu, *Chem. Mater.*, 2006, **18**, 6157–6162.
73 G. Beaucage, *J. Appl. Crystallogr.*, 1996, **29**, 134–146.
74 M. A. Elsawy, A. M. Smith, N. Hodson, A. Squires, A. F. Miller and A. Saiani, *Langmuir*, 2016, **32**, 4917–4923.
75 H. D. Glossop, G. H. De Zoysa, Y. Hemar, P. Cardoso, K. Wang, J. Lu, C. Valéry and V. Sarojini, *Biomacromolecules*, 2019, **20**, 2515–2529.
76 R. Sarroukh, E. Goormaghtigh, J. M. Ruysschaert and V. Raussens, *Biochim. Biophys. Acta, Biomembr.*, 2013, **1828**, 2328–2338.
77 S. M. Kelly, T. J. Jess and N. C. Price, *Biochim. Biophys. Acta, Proteins Proteomics*, 2005, **1751**, 119–139.
78 C. Lara, N. P. Reynolds, J. T. Berryman, A. Xu, A. Zhang and R. Mezzenga, *J. Am. Chem. Soc.*, 2014, **136**, 4732–4739.
79 A. Iyer, S. J. Roeters, V. Kogan, S. Woutersen, M. M. A. E. Claessens and V. Subramaniam, *J. Am. Chem. Soc.*, 2017, **139**, 15392–15400.
80 C. J. Bowerman and B. L. Nilsson, *J. Am. Chem. Soc.*, 2010, **132**, 9526–9527.
81 C. Diaferia, V. Roviello, G. Morelli and A. Accardo, *ChemPhysChem*, 2019, **20**, 2774–2782.
82 M. Ziaunys and V. Smirnovas, *PeerJ*, 2019, **7**, e6518.
83 C. Avitabile, C. Diaferia, V. Roviello, D. Altamura, C. Giannini, L. Vitagliano, A. Accardo and A. Romanelli, *Chem. – Eur. J.*, 2019, **25**, 14850–14857.
84 M. Groenning, *J. Chem. Biol.*, 2010, **3**, 1–18.
85 C. Xue, T. Y. Lin, D. Chang and Z. Guo, *R. Soc. Open Sci.*, 2017, **4**, 160696.
86 P. Arosio, T. P. J. Knowles and S. Linse, *Phys. Chem. Chem. Phys.*, 2015, **17**, 7606–7618.
87 C. Tang, A. M. Smith, R. F. Collins, R. V. Ulijn and A. Saiani, *Langmuir*, 2009, **25**, 9447–9453.
88 A. Pizzi, C. Pigliacelli, A. Gori, Nonappa, O. Ikkala, N. Demitri, G. Terraneo, V. Castelletto, I. W. Hamley, F. Baldelli Bombelli and P. Metrangolo, *Nanoscale*, 2017, **9**, 9805–9810.
89 Y. Wang, W. Zhang, C. Gong, B. Liu, Y. Li, L. Wang, Z. Su and G. Wei, *Soft Matter*, 2020, **16**, 10029–10045.
90 A. K. Das and P. K. Gavel, *Soft Matter*, 2020, **16**, 10065–10095.